Spin splitting with persistent spin textures induced by the line defect in the 1*T* phase of monolayer transition metal dichalcogenides

Moh. Adhib Ulil Absor* and Iman Santoso
Department of Physics, Faculty of Mathematics and Natural Sciences, Universitas Gadjah Mada, Sekip Utara BLS 21 Yogyakarta 55186, Indonesia

Naoya Yamaguchi and Fumiyuki Ishii
Nanomaterial Reserach Institute, Kanazawa University, 920-1192 Kanazawa, Japan

(Received 9 January 2020; revised manuscript received 6 March 2020; accepted 18 March 2020; published 9 April 2020)

The spin splitting driven by spin-orbit coupling in the monolayer (ML) transition metal dichalcogenide (TMDC) family has been widely studied only for the 1*H*-phase structure, while its 1*T*-phase structure has not been as widely researched due to the centrosymmetry of the crystal. Based on first-principles calculations, we show that significant spin splitting can be induced in the ML 1*T*-TMDCs by introducing the line defect. Taking the ML $PtSe_2$ as a representative example, we considered the stablest form of the line defects, namely, the Se vacancy line defect (Se-VLD). We find that large spin splitting is observed in the defect states of the Se-VLD, exhibiting a highly unidirectional spin configuration in the momentum space. This peculiar spin configuration may yield the so-called persistent spin textures (PSTs), a specific spin structure resulting in protection against spin decoherence and supporting an extraordinarily long spin lifetime. Moreover, by using $\vec{k} \cdot \vec{p}$ perturbation theory supplemented with symmetry analysis, we clarified that the emerging of the spin splitting maintaining the PSTs in the defect states originates from the inversion symmetry breaking together with the one-dimensional nature of the Se-VLD engineered ML $PtSe_2$. Our findings pave a possible way to induce significant spin splitting in the ML 1*T*-TMDCs, which could be highly important for designing spintronic devices.

DOI: 10.1103/PhysRevB.101.155410

I. INTRODUCTION

Since the experimental isolation of graphene in 2004 [1], significant research efforts have been devoted to the investigation of two-dimensional (2D) materials with atomically thin crystals [2]. Here, growing research attention has been focused on the monolayer (ML) transition metal dichalcogenide (TMDC) family due to the high possibility of being used in future nanoelectronic devices [3]. Most of the ML TMDCs families have graphenelike hexagonal crystal structures where transition metal atoms (M) are sandwiched between layers of chalcogen atoms (X) with MX_2 stoichiometry. However, due to the local coordination of the transition metal atoms, they admit two different stable forms in the ground state, namely, a 1*H*-phase structure having trigonal prismatic symmetry and a 1*T*-phase structure that consists of distorted octahedral symmetry [4]. The different coordination environments in the ML TMDCs lead to distinct crystal field splitting of the d-like bands. However, depending on the transition metal atom species, the ML TMDCs display metallic, semiconducting, or insulator behavior [5]. Therefore, various physical properties such as tunability of the band gap [6,7], high carrier mobility [8,9], and superior surface reactivity [10] are established, evidencing that the ML TMDCs are an ideal platform for next-generation technologies.

Of special interest is the promising application of the ML TMDCs for spintronics devices due to the strong spin-orbit coupling (SOC), which is particularly noticeable in the ML 1*H*-TMDCs such as ML (Mo/W)X_2 (X = S, Se) [6,11,12]. Here, the lack of the crystal inversion symmetry together with the strong SOC in the 5d orbitals of transition metal atoms leads to the large spin splitting in the electronic band structures. This effect is conspicuously apparent in the valence band maximum exhibiting spin splittings ranging between 150 meV (ML MoS_2) and 400 meV (WSe_2) [6,11,12]. Due to the well-separated valleys at the K and K' points in the hexagonal Brillouin zone, this splitting gives rise to the so-called spin-valley coupling [13], which is responsible for the appearance of valley-contrasting effects such as the spin Hall effect [14], the spin-dependent selection rule for optical transitions [15], and the magnetoelectric effect in the ML TMDCs [16]. Furthermore, an electrically controllable spin splitting and spin polarization in the ML 1*H*-TMDCs have been reported [17], making them suitable for a spin-field effect transistor.

Compared to the well-studied ML 1*H*-TMDCs, the effect of the SOC in the ML 1*T*-TMDCs is equally interesting. Especially, the ML $PtSe_2$ has attracted much scientific attention since it was successfully synthesized by direct selenization at the Pt(111) substrate [8,18]. Moreover, this material has been predicted to exhibit the largest electron mobility among the widely studied ML TMDCs [8,9]. Recently, Yao *et al.* [18], by using spin- and angle-resolved photoemission spectroscopy

*adib@ugm.ac.id

(spin-ARPES), reported spin-layer locking phenomena in the ML $PtSe_2$; that is, the spin-polarized states are degenerated in energy but spatially locked into two sublayers forming an inversion partner. A similar phenomenon has also been theoretically predicted for other ML 1T-TMDCs such as ML (Zr/Hf)X_2 (X = S, Se) [19]. This phenomenon, which is a manifestation of the global centrosymmetry of the crystal and the local dipole-induced Rashba SOC effect, may provide a disadvantage for spintronics applications. Since the ML 1T-TMDCs possess superior transport properties due to the high electron mobility [8,9], lifting the spin degeneracy in the ML 1T-TMDCs could be an important key for their realization in spintronics devices. Therefore, finding a feasible method to induce significant spin splitting in the ML 1T-TMDCs is highly desirable.

In this paper, by using density-functional theory (DFT) calculations, we show that significant spin splitting can be induced in the ML 1T-TMDCs by introducing the line defect. By using the ML $PtSe_2$ as a representative example, we investigate the stablest form of the line defects, namely, the Se-vacancy line defect (Se-VLD). We find that a sizable spin splitting is observed in the defect states of the Se-VLD, exhibiting a highly unidirectional spin configuration in momentum space. This peculiar spin configuration gives rise to the so-called persistent spin textures (PSTs) [20,21], a specific spin structure that protects the spin from decoherence and induces an extremely long spin lifetime [22,23]. Moreover, by using $\vec{k}\cdot\vec{p}$ perturbation theory supplemented with symmetry analysis, we clarified that the emergence of the spin splitting maintaining the PSTs in the defect states originates from the inversion symmetry breaking and one-dimensional (1D) nature of the Se-VLD engineered ML $PtSe_2$. Finally, a possible application of the present system for spintronics will be discussed.

II. COMPUTATIONAL DETAILS

We performed first-principles electronic structure calculations based on the DFT within the generalized gradient approximation [24] implemented in the OPENMX code [25]. Here, we adopted norm-conserving pseudopotentials [26] with an energy cutoff of 350 Ry for charge density. The wave functions are expanded by the linear combination of multiple pseudoatomic orbitals generated using a confinement scheme [27,28]. The orbitals are specified by Pt7.0-$s^2p^2d^2$ and Se9.0-$s^2p^2d^1$, which means that the cutoff radii are 7.0 and 9.0 bohrs for the Pt and Se atoms, respectively, in the confinement scheme [27,28]. For the Pt atom, two primitive orbitals expand the s, p, and d orbitals, while, for the Se atom, two primitive orbitals expand the s and p orbitals, and one primitive orbital expands the d orbital. The SOC was included in the DFT calculations by using j-dependent pseudopotentials [29]. The spin textures in momentum space were calculated using the spin density matrix of the spinor wave functions obtained from the DFT calculations that we applied recently to various 2D materials [30,31].

To model the VLD in the ML 1T-TMDCs, we considered the ML $PtSe_2$ as a representative example. Here, we constructed a supercell of the pristine ML $PtSe_2$ from the minimum rectangular cell [Fig. 1(a)], where the optimized lattice parameters are obtained from the primitive hexagonal cell. As a consequence, the folding cell from the hexagonal to rectangular cells in the first Brillouin zone (FBZ) is expected, as shown in Figs. 1(b) and 1(c). Here, we use the axis system where the ML is chosen to sit on the x-y plane, where the x (y) axis is taken to be parallel to the zigzag (armchair) direction. We considered two different configurations of the VLD, namely, the Se-VLD and Pt-VLD, whose relaxed structures are displayed in Figs. 1(d) and 1(e), respectively. To model these VLDs, we extend the supercell size of the ML $PtSe_2$ ten times in the x direction, which is perpendicular to the direction of the extended vacancy line along the y direction to eliminate interaction between the periodic images of the line defect [see Figs. 1(d) and 1(e)].

In our DFT calculations, we used a periodic slab where a sufficiently large vacuum layer (20 Å) is used to avoid interaction between adjacent layers. The $3\times12\times1$ k-point mesh was used, and the geometries were fully relaxed until the force acting on each atom was less than 1 meV/Å. To confirm the energetic stability of the VLD, we calculate the vacancy formation energy E_f through the following relation [32]:

$$E_f = E_{\mathrm{VLD}} - E_{\mathrm{Pristine}} + \sum_i n_i\mu_i. \tag{1}$$

In Eq. (1), E_{VLD} is the total energy of the VLD, E_{Pristine} is the total energy of the pristine system, n_i is the number of atoms being removed from the pristine system, and μ_i is the chemical potential of the removed atoms corresponding to the chemical environment surrounding the system. Here, μ_i obtains the following requirements:

$$E_{\mathrm{PtSe_2}} - 2E_{\mathrm{Se}} \leqslant \mu_{\mathrm{Pt}} \leqslant E_{\mathrm{Pt}}, \tag{2}$$

$$\tfrac{1}{2}\left(E_{\mathrm{PtSe_2}} - E_{\mathrm{Pt}}\right) \leqslant \mu_{\mathrm{Se}} \leqslant E_{\mathrm{Se}}. \tag{3}$$

Under the Se-rich condition, μ_{Se} is the energy of the Se atom in the bulk phase (hexagonal Se, $\mu_{\mathrm{Se}} = \frac{1}{3}E_{\mathrm{Se-hex}}$), which corresponds to the lower limit on Pt, $\mu_{\mathrm{Pt}} = E_{\mathrm{PtSe_2}} - 2E_{\mathrm{Se}}$, where $E_{\mathrm{PtSe_2}}$ is the total energy of the ML $PtSe_2$ in the primitive unit cell. On the other hand, in the case of the Pt-rich condition, μ_{Pt} is associated with the energy of the Pt atom in the bulk phase (fcc Pt, $\mu_{\mathrm{Pt}} = \frac{1}{4}E_{\mathrm{Pt-fcc}}$) corresponding to the lower limit on Se, $\mu_{\mathrm{Se}} = \frac{1}{2}(E_{\mathrm{PtSe_2}} - E_{\mathrm{Pt}})$.

III. RESULTS AND DISCUSSION

First, we briefly discuss the structural symmetry and electronic properties of the pristine ML $PtSe_2$. The ML $PtSe_2$ crystallizes in a centrosymmetric crystal associated with the ML 1T-TMDCs with the $P\bar{3}mI$ space group for the global structure. Here, one Pt atom (or Se atom) is located on top of another Pt atom (or Se atom), forming octahedral coordination, while it shows trigonal structure when projected to the (001) plane [Fig. 1(a)]. As a result, a polar group, C_{3v}, and a centrosymmetric group, D_{3d}, are identified for the Se and Pt sites, respectively. We find that the calculated lattice constant of the pristine ML $PtSe_2$ in the primitive unit cell is 3.75 Å, which is in good agreement with previous theoretical (3.75 Å [33,34]) and experimental (3.73 Å [8]) results.

Figure 2(a) shows the calculated result of the electronic band structures of the (1×1) primitive unit cell of the pristine

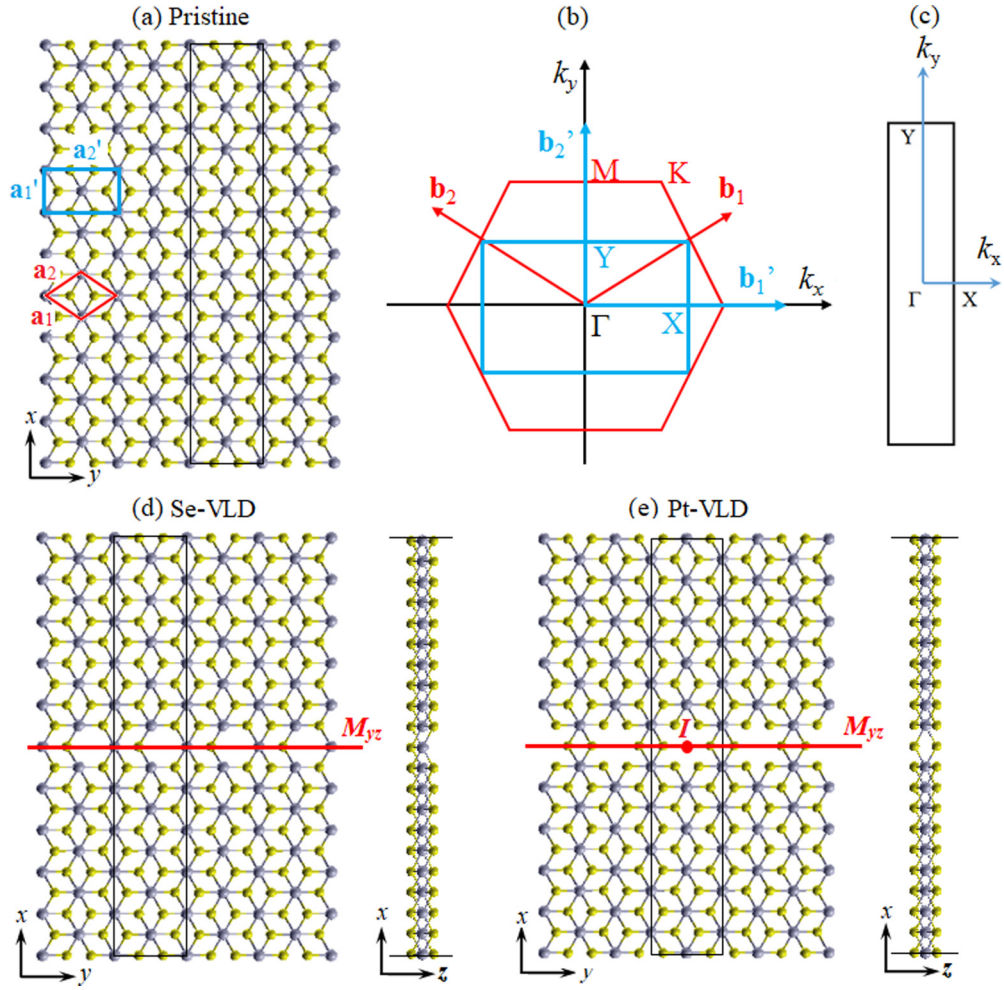

FIG. 1. (a) Top view of the crystal structures of the pristine ML $PtSe_2$, where red, blue, and black lines represent the primitive hexagonal cell, minimum rectangular cell, and rectangular supercell, respectively, corresponding to (b) the folding of the FBZ between primitive hexagonal and minimum rectangular cells. (c) The FBZ for the pristine supercell is also shown. Top and side views of the crystal for (d) the Se vacancy line defect (Se-VLD) and (e) the Pt vacancy line defect (Pt-VLD). Both line defects are oriented along the armchair direction (y direction), while they are isolated in the direction perpendicular to the line defect (x direction), as indicated by black lines of the rectangular lattice. Here, all of the symmetry operations, including the inversion symmetry I and mirror symmetry M_{yz}, are indicated by the red point and lines.

ML $PtSe_2$. Consistent with previous results [8,34], we find that the pristine ML $PtSe_2$ is an indirect semiconductor with a band gap of 1.38 eV, where the valence band maximum (VBM) is located at the Γ point, while the conduction band minimum (CBM) is located at $\vec{k}$ along the Γ-M line. Our calculated results for the density of states projected to the atomic orbitals confirmed that the VBM is predominantly contributed by the Se p orbitals, while the CBM mainly originates from the Pt d orbitals [Fig. 2(b)]. Including the SOC in the calculations is expected to induce lifting of the spin degeneracy in the electronic band structure, which is driven by the lack of the inversion symmetry [35,36]. However, in the ML $PtSe_2$, we find that all the bands are doubly degenerate, which is protected by the centrosymmetry of the crystal [Fig. 2(c)]. Evidently, the spin degeneracy observed in the electronic band structures of the pristine ML $PtSe_2$ is consistent with the recent experimental results reported by Yao *et al.* using spin-ARPES [18].

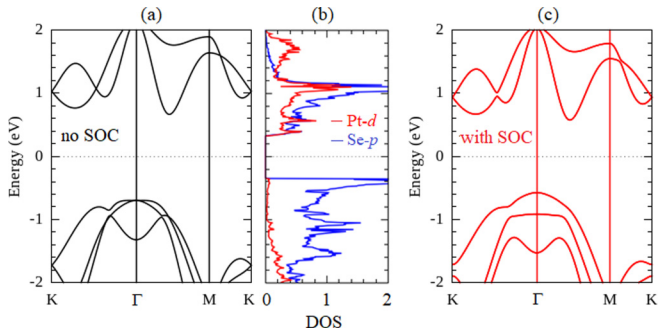

FIG. 2. (a) Electronic band structure of the pristine ML $PtSe_2$ calculated without the spin-orbit coupling (SOC) corresponding to (b) density of states projected to the atomic orbitals. (c) the electronic band structures calculated with including the SOC.

When the VLD is introduced, the position of the atoms around the VLD site significantly changes from that of the pristine atomic position due to the relaxation. To examine

TABLE I. The calculated vacancy formation energy E_f of the Se-VLD and Pt-VLD in the ML $PtSe_2$ corresponding to the Pt-Se bond length d_{Pt-Se} around the vacancy site, compared with that of the single vacancy defect (Se-SVD and Pt-SVD) and the pristine systems. Some theoretical data for the SVD systems from previous reports are presented for a comparison.

Defective systems	E_f (eV)	d_{Pt-Se} (Å)	Reference
Pristine		2.548	This work
Se-VLD	1.92 (Se-rich); 1.46 (Pt-rich)	2.553	This work
Pt-VLD	4.85 (Se-rich); 4.11 (Pt-rich)	2.576	This work
Se-SVD	1.78 (Se-rich); 1.35 (Pt-rich)	2.509	This work
	1.84 (Se-rich); 1.27 (Pt-rich)	2.509	Ref. [37]
	1.87 (Se-rich); 1.24 (Pt-rich)		Ref. [34]
Pt-SVD	4.35 (Se-rich); 3.11 (Pt-rich)	2.508	This work
	4.28 (Se-rich); 3.06 (Pt-rich)	2.508	Ref. [37]
	4.19 (Se-rich); 3.00 (Pt-rich)		Ref. [34]

the optimized structures of the VLD, we show the calculated results of the Pt-Se bond length d_{Pt-Se} around the VLD site in Table I. In the case of the Se-VLD, removing one Se atom from the supercell breaks the inversion symmetry I of the ML $PtSe_2$ [Fig. 1(d)]. Consequently, three Pt atoms around the VLD site are relaxed and move close to each other, implying that d_{Pt-Se} at each hexagonal side around the VLD site has the same value of about 2.553 Å. As a result, a mirror symmetry plane M_{yz} exists along the extended vacancy line [Fig. 1(d)]. In contrast to the Se-VLD case, the Pt-VLD retains both the inversion symmetry I and mirror symmetry M_{yz} in the supercell [Fig. 1(e)]. However, the geometry of the Pt-VLD undergoes significant distortion from the pristine crystal, resulting in d_{Pt-Se} of the Pt-VLD (2.576 Å) being slightly larger than those of the Se-VLD (2.553 Å) and pristine (2.548 Å) systems.

To assess the stability of the proposed VLDs, we calculate their formation energy E_f. As shown in Table I, we find that the calculated E_f of the Se-VLD is much smaller than that of the Pt-VLD under the Se-rich and Pt-rich conditions, indicating that the Se-VLD is easily formed in the ML $PtSe_2$. In contrast, the formation of the Pt-VLD is highly unfavorable due to the required energy. Since the Pt atom is covalently bonded to the six neighboring Se atoms, removing the Pt atom in the supercell is stabilized by increasing E_f. For comparison, we also calculate E_f of a Se single vacancy defect (Se-SVD) and a Pt single vacancy defect (Pt-SVD) by using the same supercell model. We find that the calculated E_f of the Se-VLD is comparable to that of the Se-SVD but is much smaller than that of the Pt-SVD (see Table I), suggesting that the formation of the Se-VLD is energetically accessible. The determined stability of the Se-VLD is consistent with the previous report that the chalcogen vacancies and their alignment in the extended line defects can easily be formed in the ML TMDCs [34,37–40]. In fact, aggregation of the chalcogen vacancy and their alignment in the extended line defect was experimentally reported on ML MoS_2 by using the electron irradiation technique [41–43], indicating that the Se-VLD engineered ML $PtSe_2$ is experimentally feasible. Since the Se-VLD has the lowest formation energy in the VLD systems, in the following discussion, we will concentrate only on the electronic properties of the Se-VLD engineered ML $PtSe_2$.

Figures 3(a) and 3(b) show the band structures of the Se-VLD along the Γ-X-Γ and Γ-Y-Γ lines in the FBZ, respectively, corresponding to the electronic wave function [Figs. 3(c)–3(e)] at the Γ point around the Fermi level. Without the SOC, we identify three defect levels inside the band gap, which is characterized by a single occupied defect state (DS-1) and two unoccupied defect states (DS-2 and DS-3). Our spin-polarized calculations for the Se-VLD system confirmed that there is no lifting of the spin degeneracy in the defect states, indicating that the Se-VLD engineered ML $PtSe_2$ remains nonmagnetic like the defect-free one. The observed defect states, together with the nonmagnetic character of the Se-VLD engineered ML $PtSe_2$, are consistent with previous results of a single chalcogen vacancy in various ML TMDCs [37,39,40]. Importantly, we observe a dispersive character of the bands in the defect states, which is visible in the Γ-Y direction [Fig. 3(b)]. However, the bands are dispersionless in the defect states along the Γ-X direction [Fig. 3(a)]. A similar dispersive character is also observed for the bulk bands located far from the Fermi level. The dispersionless defect states along the Γ-X direction occur because the Se-VLDs are completely isolated far from each other in the direction perpendicular to the vacancy line [see Fig. 1(d)]. On the other hand, the interaction between the neighboring vacancies along the extended vacancy line induces a delocalized wave function, forming a quasi-1D confined state along the vacancy line direction [Figs. 3(c)–3(e)]. Such a peculiar wave function is responsible for inducing the dispersive defect states along the Γ-Y direction, which is expected to enhance carrier mobility [44], and thus plays an important role in the transport-based electronic devices.

Taking into account the SOC in the calculations gives rise to the spin-split bands in the defect states since the inversion symmetry of the ML $PtSe_2$ is broken by the formation of the Se-VLD. However, as shown in Figs. 3(a) and 3(b), we find that the spin splitting in the defect states is highly anisotropic. Due to the 1D confined states along the extended vacancy line [Figs. 3(c)–3(e)], significant spin splitting is forced to occur in the defect states along the Γ-Y direction [Fig. 3(b)]. However, an extremely small (nearly zero) spin splitting remains in the defect states along the Γ-X direction [Fig. 3(a)] and is completely degenerate when the supercell size perpendicular to the extended vacancy line is increased (see Figs. S1 and S2 in Supplemental Material for details [45]). Since the spin splitting is preserved only along the Γ-Y line (k_y direction), an ideal 1D SOC is achieved, which is expected to induce a high spin coherency, as recently predicted for the 1D topological defect induced by screw dislocation in semiconductors [46], and hence is promising for spintronic applications. Later on, we will show that such typical SOC is reflected by our SOC Hamiltonian derived from the $\vec{k} \cdot \vec{p}$ perturbation theory and symmetry analysis.

Although the spin splitting in the defect states is subjected to the structural symmetry and the 1D nature of the Se-VLD engineered ML $PtSe_2$, it is expected that orbital hybridizations in the defect states play an important role. Here, coupling between atomic orbitals contributes to the nonzero SOC matrix element through the relation $\zeta_l \langle \vec{L} \cdot \vec{S} \rangle_{u,v}$, where ζ_l is angular

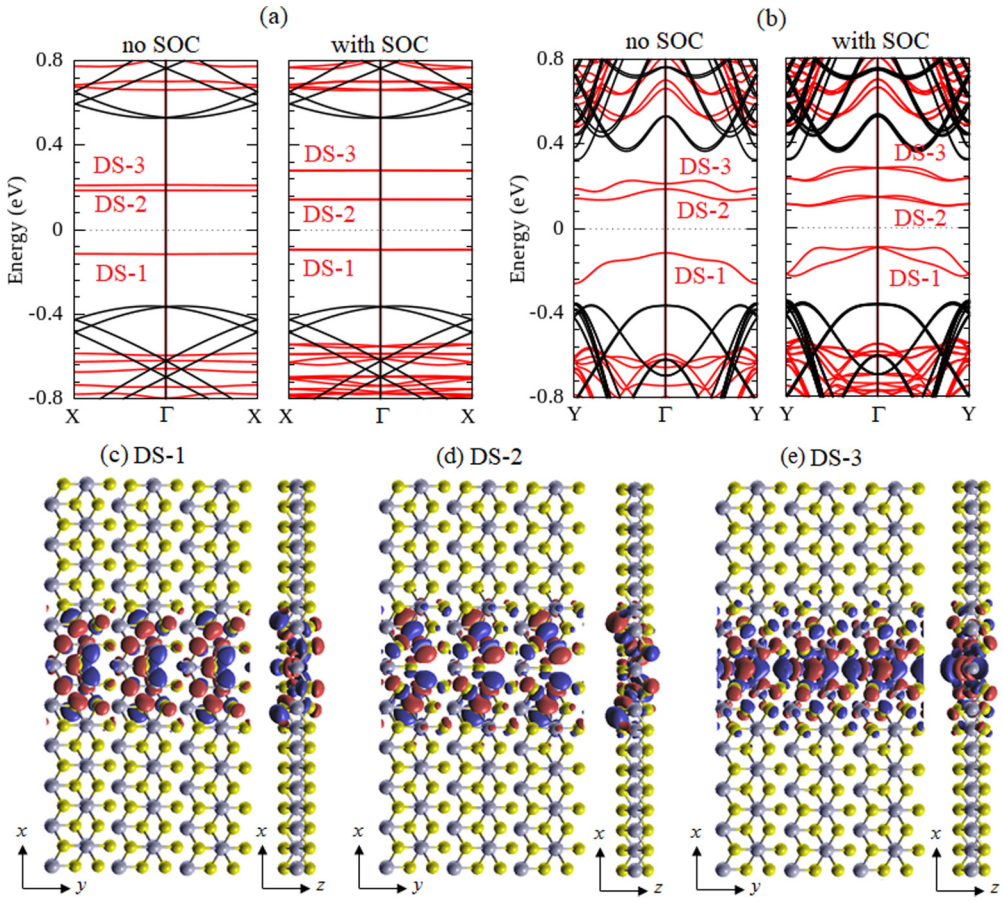

FIG. 3. Band structures calculated along the (a) X-Γ-X and (b) Y-Γ-Y directions for the Se-VLD (red lines) compared with those of the pristine supercell systems (black lines) without (left) and with (right) including the SOC. Here, DS-1 indicates an occupied defect state, while DS-2 and DS-3 represent the two unoccupied defect states. Isosurface map of the wave function calculated at the Γ point for (c) the DS-1, (d) DS-2, and (e) DS-3 defect states, where the isovalue of the wave function is 0.02 $e/\text{Å}^3$.

momentum resolved atomic SOC strength, with $l = (s, p, d)$, $\vec{L}$ and $\vec{S}$ are the orbital angular momentum and Pauli spin operators, and (u, v) is the atomic orbitals. Therefore, only the orbitals with a nonzero magnetic quantum number ($m_l \neq 0$) will contribute to the spin splitting. By calculating the orbital-resolved electronic band structures projected to the atom around the VLD site, we find that large spin splitting in the defect states mostly originates from the contribution of the $p_x + p_y$ ($m_l = \pm 1$) orbital of the next-nearest-neighbor and nearest-neighbor Se atoms and the $d_{x^2-y^2} + d_{xy}$ ($m_l = \pm 2$) orbital of the Pt atom (Fig. 4). This result is consistent with previous calculations [37,40] that introducing a chalcogen vacancy in the ML TMDCs leads to significant in-plane p-d orbital coupling, which plays an important role in inducing the large spin splitting in the defect states.

To further demonstrate the nature of the observed spin splitting in the defect states of the Se-VLD engineered ML $PtSe_2$, we show the calculated spin textures around the Γ point in Fig. 5(a) for the occupied defect state (DS-1) and in Figs. 5(b) and 5(c) for the unoccupied defect states (DS-2, DS-3). It is clearly seen that the spin textures for the upper and lower branches of the spin-split defect states (DS-1, DS-2, DS-3) exhibit a uniform spin configuration along the x direction except for $k_y = 0$, indicating that the spin polarization is dominated by the σ_x component of spins. However, the spin orientation is fully reversed when the k_y component of the wave vector is changed to $-k_y$ due to time-reversal symmetry. We reveal that there is no deviation of the spin orientation even at large k_y, indicating that the spin textures are highly unidirectional. This peculiar pattern of the spin textures gives rise to the so-called persistent spin textures [20,21], protecting the spin from the decoherence through the Dyakonov-Perel spin-relaxation mechanism [22,23]. Accordingly, an extremely long spin lifetime is expectable, offering a promising platform to realize an efficient spintronics device. Previously, the PSTs were widely studied for semiconductor quantum well (QW) heterostructures [47–50]. However, achieving the PSTs in these materials requires a stringent condition for fine tuning equal Rashba and Dresselhaus (RD) SOC parameters [20,21], which is practically nontrivial. On the other hand, only a few materials are predicted to maintain the PSTs intrinsically, as recently reported for bulk $BiInO_3$ [51], $CsBiNb_2O_7$ [52], the ZnO (10-10) surface [53], and newly reported 2D materials, including ML WO_2Cl_2 [54] and ML group-IV monochalcogenides [30,31]. Therefore, our finding of the PSTs in the Se-VLD engineered ML $PtSe_2$ may provide a distinct advantage over the widely studied PST materials, albeit available intrinsically in a single material.

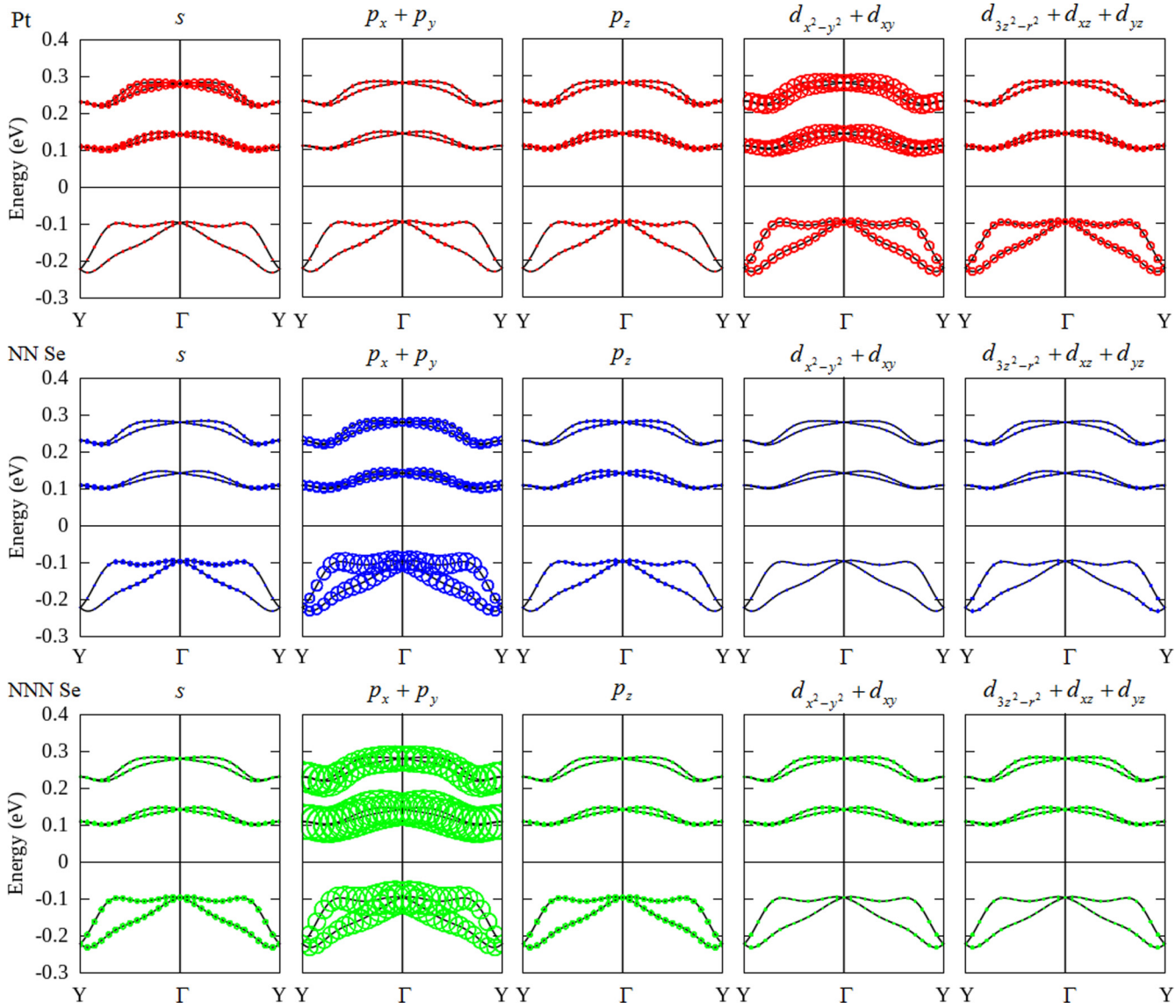

FIG. 4. Orbital-resolved electronic band structures calculated at the defect states projected to the Pt (red circles), nearest-neighbor (NN) Se (blue circles), and next-nearest-neighbor (NNN) Se (green circles) atoms. The radii of the circles reflect the magnitude of the spectral weight of the particular orbitals to the bands.

To understand the origin of the observed spin splitting and PSTs in the defect states of the Se-VLD engineered ML $PtSe_2$, we derive a minimal SOC Hamiltonian $\hat{H}_{\rm SOC}$ by using $\vec{k}\cdot\vec{p}$ perturbation theory combined with symmetry analysis. Although the inversion symmetry is absent in the Se-VLD, its time-reversal symmetry is conserved at the high-symmetry point in the FBZ such as the $\Gamma(0,0,0)$ and $Y(0,\pm 0.5,0)$ points, leading to the fact that the spin degeneracy remains. When the SOC is introduced, the spin degeneracy is lifted at $\vec{k}$ away from the time-reversal-invariant points, in which $\hat{H}_{\rm SOC}$ can be derived by $\vec{k}\cdot\vec{p}$ theory. Following Vajna *et al.*, it is possible to construct $\hat{H}_{\rm SOC}$ from the following invariance formula [55]:

$$H_{\rm SOC}(\vec{k}) = \alpha(g\vec{k})\cdot[\det(g)g\vec{\sigma}], \tag{4}$$

where $\vec{k}$ and $\vec{\sigma}$ are the electron's wave vector and spin vector, respectively, and $\alpha(g\vec{k}) = \det(g)g\alpha(\vec{k})$, where g is the element of the point group characterizing the small group wave vector G_Q of the high-symmetry point Q in the FBZ. In Eq. (4), we have implicitly assumed that all of the orbital characters at the Q point are invariant under the symmetry transformation in G_Q. Therefore, the spin vector $\vec{\sigma}$ can be considered a pseudovector. By transforming $\vec{k}$ and $\vec{\sigma}$ as polar and axial vectors, respectively, and sorting out the components of these vectors according to irreducible representation (IR) of $G_{\bar{Q}}$, we can decompose again their direct product into the IR. According to Eq. (4), only the total symmetric IR from this decomposition contributes to $\hat{H}_{\rm SOC}$. Therefore, by using the corresponding tables of the point group, one can easily construct the possible terms of $\hat{H}_{\rm SOC}$.

In the Se-VLD engineered ML $PtSe_2$, the structural symmetry is characterized by only the mirror symmetry operation $M_{yz}:(x,y,z)\rightarrow(-x,y,z)$ and hence belongs to the C_s point group. Therefore, the small group of the wave vector at the Γ point also belongs to the C_s point group. Due to the 1D nature

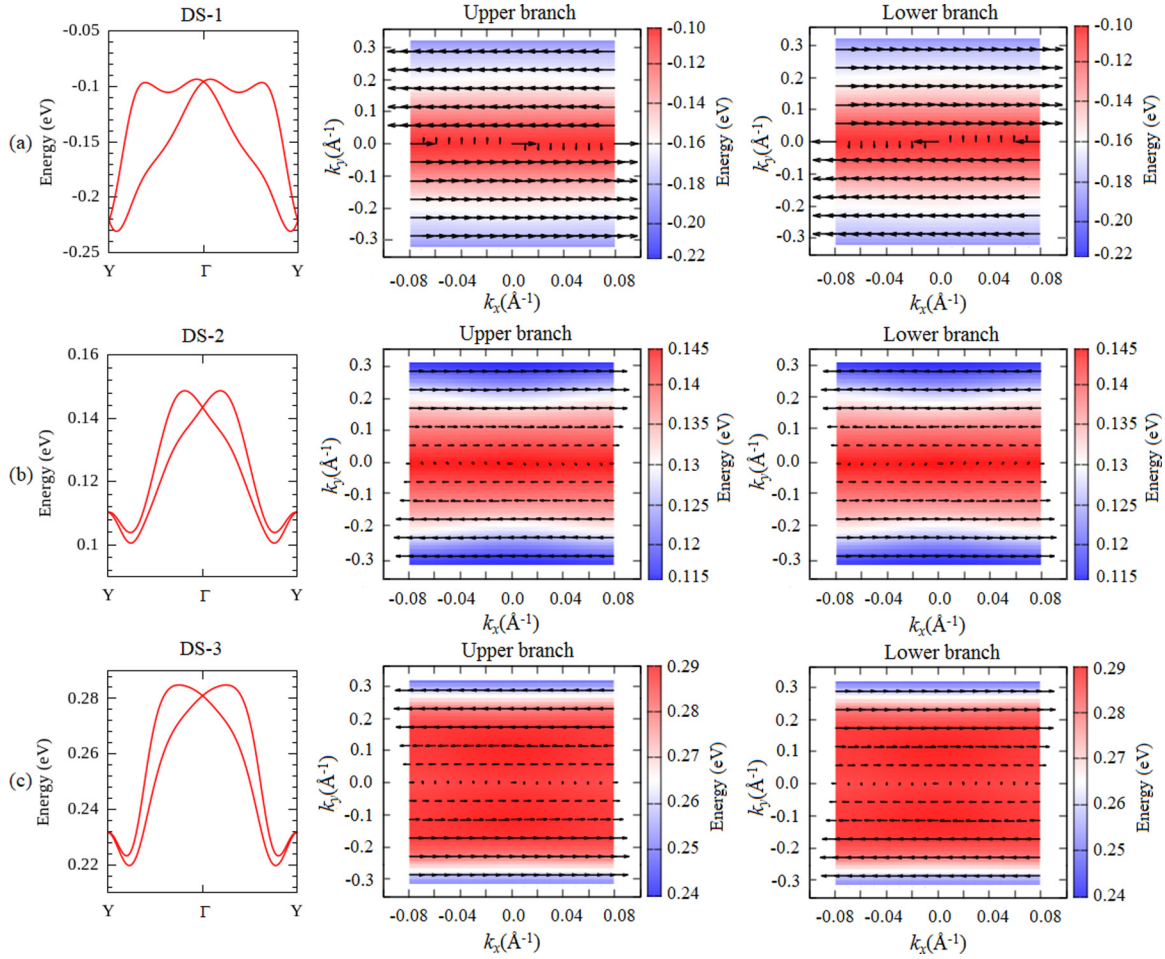

FIG. 5. Spin-split bands of the defect states along the Y-Γ-Y line corresponding to the spin textures in momentum space for (a) DS-1, (b) DS-2, and (c) DS-3. The color scales represent the energy of the band near the defect states, while the black arrows indicate the orientation of the spin polarization in the momentum k space.

of the wave function in the defect states [Figs. 3(c)–3(e)], the orbital characters of the wave function are imposed to be invariant under all symmetry operations in the C_s point group. Accordingly, $\vec{\sigma}$ can be viewed as a pseudovector, which allows us to apply Eq. (4) to derive $\hat{H}_{\rm SOC}$. On the basis of the character table of the C_s point group (see Table II), we sort out the components of $\vec{k}$ and $\vec{\sigma}$ according to the IRs as k_y, k_z, and σ_x for A' and k_x, σ_y, and σ_z for A''. Moreover, from the corresponding table of direct products (Table III), we obtain the third-order terms of $\vec{k}$ as k_y^3, k_z^3, $k_y^2k_z$, $k_x^2k_z$, and $k_z^2k_y$ for A' and k_x^3, $k_y^2k_x$, $k_yk_xk_z$, and $k_z^2k_x$ for A''. However, due to the 1D nature of the defect, all the terms containing k_x and k_z should vanish. Therefore, according to the table of direct products, the combination of the first order of $\vec{k}$ and the third order of k^3 with $\vec{\sigma}$ that belongs to the A' IR is $k_y\sigma_x$ and $k_y^3\sigma_x$. This combination can be generalized for the higher odd nth order of $\vec{k}$, where the only nonzero term is $k_y^n\sigma_x$. By collecting all these terms, we obtain $\hat{H}_{\rm SOC}$ near the Γ point as

$$H_{\rm SOC}(\vec{k}) = \alpha_1 k_y\sigma_x + \alpha_3 k_y^3\sigma_x + \alpha_5 k_y^5\sigma_x + \cdots + \alpha_n k_y^n\sigma_x, \quad (5)$$

where α_n is the odd nth-order SOC parameter.

It is revealed by Eq. (5) that $\hat{H}_{\rm SOC}$ is characterized only by one component of the wave vector, k_y, and the spin vector σ_x. Therefore, $\hat{H}_{\rm SOC}$ preserves an ideal 1D SOC, as recently predicted for the 1D topological defect induced by

TABLE II. Character table for the C_s point group with two elements of the symmetry operation, namely, the identity operation $E : (x, y, z) \rightarrow (x, y, z)$ and the mirror symmetry operation $M_{yz} : (x, y, z) \rightarrow (-x, y, z)$. Two one-dimensional irreducible representations (IRs) are shown.

IRs	E	M_{yz}	Linear, rotation
A'	1	1	y, z, R_x
A''	1	−1	x, R_y, R_z

TABLE III. Direct product table of the irreducible representations for the C_s point group.

	A'	A''
A'	A'	A''
A''	A''	A'

TABLE IV. Linear term parameter of the SOC Hamiltonian α_1 and the wavelength of the PSH λ calculated on the defect states (DS-1, DS-2, DS-3) of the Se-VLD engineered ML $PtSe_2$ compared with those observed on various PSH materials.

Systems	α_1 (eV Å)	λ_{PST} (nm)	Reference
Se-VLD in ML $PtSe_2$			
DS-1	1.14	6.33	This work
DS-2	0.20	29.47	This work
DS-3	0.28	28.19	This work
Interface			
GaAs/AlGaAs	$(3.5–4.9)\times10^{-3}$	$(7.3–10)\times10^{3}$	[47]
	2.77×10^{-3}	5.5×10^{3}	[48]
InAlAs/InGaAs	1.0×10^{-3}		[50]
	2.0×10^{-3}		[49]
Strained $LaAlO_3/SrTiO_3$	31.5×10^{-3}	98	[56]
Surface			
ZnO(10-10) surface	34.78×10^{-3}	1.9×10^{2}	[53]
Bulk			
$BiInO_3$	1.91	2.0	[51]
$CsBiNb_2O_7$	0.012–0.014		[52]
2D ML systems			
MX (M = Sn, Ge; X = S, Se, Te)	0.09–1.7	$1.82–1.5\times10^{2}$	[31]
Halogen-doped SnSe	1.6–1.76	1.2–1.41	[30]
WO_2Cl_2	0.9		[54]

screw dislocation in semiconductors [46]. Accordingly, the spin splitting is expected to occur only along the k_y direction (Γ-Y line), which is in agreement with the band dispersion in Fig. 3(b) obtained from our DFT calculations. On the other hand, it is clearly seen from Eq. (5) that the only nonzero spin component in $\hat{H}_{SOC}$ is σ_x, indicating that the spin orientation is collinear to the x axis and thus maintaining the PSTs. Importantly, the 1D nature of the SOC found in $\hat{H}_{SOC}$ is conserved up to the higher-order term of k_y, indicating that the formation of the PSTs remains at the larger k_y without any deviation of the spin polarization, which is very consistent with the highly unidirectional spin textures shown in Figs. 5(a)–5(c).

We highlight the main difference of our derived $\hat{H}_{SOC}$ given in Eq. (5) from the widely studied 2D RD SOC effect supporting the PSTs. In the 2D RD-SOC, the SOC Hamiltonian can be expressed as $\hat{H}_{SOC} = \vec{\Omega}\cdot\vec{\sigma}$, where $\vec{\Omega}$ is the spin-orbit field (SOF), defined as $\vec{\Omega} = (\alpha_R k_y + \alpha_D k_x, -\alpha_R k_x - \alpha_D k_y, 0)$, with α_R and α_D being the Rashba and Dresselhaus SOC parameters, respectively. Such SOC leads to a chiral spin texture characterized by the spin-momentum-locking property, which is known to induce the undesired effect of causing spin decoherence [22]. The PSTs occur when the SOF $\vec{\Omega}$ is unidirectional, which can be achieved, in particular, if the magnitudes of α_R and α_D are equal [20,21], as previously observed in conventional semiconductor QW heterostructures [47–50]. However, the condition of $\alpha_R = \beta_D$ is difficult to satisfy since it requires matching the QW width and doping level and the application of an external gate bias. On the other hand, the formation of the PSTs driven by the 2D RD-SOC is generally broken by a higher-order term of k [47,50], which has the considerable effect of reducing the spin coherency. In contrast, for our derived $\hat{H}_{SOC}$ in Eq. (5), the 1D nature of the SOC enforces the SOF always being unidirectional in the x direction whatever the order of k_y is. Therefore, the PST remains even at the larger k_y, giving an advantage to the significantly higher degree of spin coherency than that of the 2D RD-SOC.

For a quantitative analysis of the predicted PST in the Se-VLD engineered ML $PtSe_2$, we calculate the SOC parameter α_1 associated with the linear term of $\hat{H}_{SOC}$ given in Eq. (5) and compare the result with a few selected PSH materials. By fitting the DFT bands of the defect states along the Γ-Y line, we find that the calculated α_1 for the DS-1 state is 1.14 eV Å, which is larger than those for the DS-2 state (0.20 eV Å) and the DS-3 state (0.28 eV Å; see Table IV). However, this value is much larger than those of the semiconductor QW systems such as GaAs/AlGaAs [47,48] and InAlAs/InGaAs [49,50], the ZnO (10-10) surface [53], and the strained $LaAlO_3/SrTiO_3$ (001) interface [56]. Still, this value is comparable to that of the bulk $CsBiNb_2O_7$ [52], $BiInO_3$ [51], and newly reported 2D materials, including the ML WO_2Cl_2 [54] and ML group-IV monochalcogenides [30,31] (see Table IV). Remarkably, the associated SOC parameters found in the defect states of the Se-VLD engineered ML $PtSe_2$ are sufficient to support the room temperature spintronics functionality.

The observed PST in our defective system may result in a spatially periodic mode of the spin polarization emerging in the crystal known as a persistent spin helix [PSH] [21]. The corresponding spin-wave mode is characterized by a wavelength of $\lambda = (\pi\hbar^2)/(m^*_{\Gamma-Y}\alpha_1)$ [21], where $m^*_{\Gamma-Y}$ is the carrier effective mass along the Γ-Y direction. By fitting the band dispersion in the defect states along the Γ-Y line, we find that the calculated $m^*_{\Gamma-Y}$ is $-0.21m_0$ for the DS-1 state, while it is found to be $0.25m_0$ and $0.19m_0$ for the DS-2 and DS-3 states, respectively, where m_0 is the free-electron mass. The negative (positive) value of $m^*_{\Gamma-Y}$ characterizes the effective mass of the hole (electron) carriers in the occupied (unoccupied) defect states. The resulting wavelength λ is 6.33 nm for the DS-1 state, which is one order smaller than that for the

DS-2 (29.47 nm) and DS-3 (28.12 nm) states (see Table IV). Specifically, the calculated λ for the DS-1 state is comparable to that reported for the bulk $BiInO_3$ [51] and ML group-IV monochalcogenides [30,31] (see Table IV), rendering the present system promising for nanoscale spintronics devices.

Thus far, we have found that the PST is achieved in the defect states of the Se-VLD engineered ML $PtSe_2$. In particular, the PST with the largest strength of the spin splitting ($\alpha_1 = 1.14$ eV Å) is observed in the DS-1 state, indicating that the PSH will be formed when the hole carriers are optically injected into the occupied defect state of the Se-VLD engineered ML $PtSe_2$. Since the wavelength of the PSH in the DS-1 state ($\lambda = 6.33$ nm) is very small, it is possible to resolve the features down to the tens of nanometers scale with subnanosecond time resolution by using near-field scanning Kerr microscopy [57]. In addition, due to the sizable spin splitting in the DS-1 state, the two states with opposite spin orientations at k_y and $-k_y$ are expected to induce large Berry curvature with opposite signs. By using a polarized optical excitation technique, it is possible to create different hole populations between these two states. Therefore, a charge Hall current similar to the valley Hall effect recently discovered in TMDCs can be measured [58]. As such, our findings for the large spin splitting in the Se-VLD engineered ML $PtSe_2$ maintaining the PST are useful for spintronic applications.

IV. CONCLUSION

The effect of the line defect on the electronic properties of the ML 1T-TMDCs has been systematically investigated by employing first-principles DFT calculations. Taking the ML $PtSe_2$ as a representative example, we have considered the stablest form of the vacancy line defects, namely, the Se-VLD. Our band structures analysis has shown that the midgap defect states are observed in the Se-VLD, exhibiting the dispersive character of the bands along the Γ-Y direction. By taking into account the SOC in the DFT calculations, we have revealed a sizable spin splitting in the defect states of the Se-VLD, which is mainly derived from the strong hybridization between the in-plane p-d orbitals. Importantly, we have observed a highly unidirectional spin configuration in the spin-split defect states, giving rise to the so-called persistent spin textures [20,21], which protect the spin from decoherence and induce an extraordinarily long spin lifetime. Moreover, by using $\vec{k} \cdot \vec{p}$ perturbation theory supplemented with symmetry analysis, we have demonstrated that the emerging of the spin splitting maintaining the PST in the defect states is subjected to inversion symmetry breaking together with the 1D nature of the Se-VLD engineered ML $PtSe_2$. Recently, the defective ML 1T-TMDCs were extensively studied [33,34,37,59]. Our study clarifies that the line defect plays an important role in the spin-splitting properties of the ML 1T-TMDCs, which could be highly important for designing spintronic devices.

We emphasized here that our proposed approach for inducing the large spin splitting by using the line defects is not limited to the ML $PtSe_2$ but also can be extended to other ML 1T-TMDCs systems such as the ML PdX_2 (X= S, Se, Te) [59], ML SnX_2 [60], ML ReX_2 [61], and ML (Zr/Hf)X_2 [19], where the structural and electronic structure properties are similar. Recently, manipulation of the electronic properties of these particular materials by introducing the defect was reported [59]. Therefore, it is expected that our predictions will stimulate further theoretical and experimental efforts in the exploration of the spin splitting properties of the ML TMDCs, broadening the range of 2D materials for future spintronic applications.

ACKNOWLEDGMENTS

M.A.U.A. would like to thank the Nanomaterial Research Institute, Kanazawa University, Japan, for providing financial support during his research visit. This work was partly supported by Grants-in-Aid for Scientific Research (Grant No. 16K04875) from JSPS and Grant-in-Aid for Scientific Research on Innovative Areas Discrete Geometric Analysis for Materials Design (Grant No. 18H04481) from MEXT Japan. This work was also partly supported by a PDUPT Research Grant (2020) funded by RISTEK-BRIN, Republic of Indonesia. M.A.U.A and I.S would like to thanks RISTEK-BRIN for partially support through World Class University (WCU) Program managed by ITB. The computation in this research was performed using the supercomputer facilities at RIIT, Kyushu University, Japan.

[1] K. S. Novoselov, A. K. Geim, S. V. Morozov, D. Jiang, Y. Zhang, S. V. Dubonos, I. V. Grigorieva, and A. A. Firsov, Science **306**, 666 (2004).
[2] C. Tan, X. Cao, X.-J. Wu, Q. He, J. Yang, X. Zhang, J. Chen, W. Zhao, S. Han, G.-H. Nam, M. Sindoro, and H. Zhang, Chem. Rev. **117**, 6225 (2017).
[3] S. Manzeli, D. Ovchinnikov, D. Pasquier, O. V. Yazyev, and A. Kis, Nat. Rev. Mater. **2**, 17033 (2017).
[4] P. Cudazzo, M. Gatti, and A. Rubio, Phys. Rev. B **90**, 205128 (2014).
[5] J. Wilson and A. Yoffe, Adv. Phys. **18**, 193 (1969).
[6] M. A. U. Absor, H. Kotaka, F. Ishii, and M. Saito, Phys. Rev. B **94**, 115131 (2016).
[7] A. Ramasubramaniam, D. Naveh, and E. Towe, Phys. Rev. B **84**, 205325 (2011).
[8] Y. Wang, L. Li, W. Yao, S. Song, J. T. Sun, J. Pan, X. Ren, C. Li, E. Okunishi, Y.-Q. Wang, E. Wang, Y. Shao, Y. Y. Zhang, H.-T. Yang, E. F. Schwier, H. Iwasawa, K. Shimada, M. Taniguchi, Z. Cheng, S. Zhou, S. Du, S. J. Pennycook, S. T. Pantelides, and H.-J. Gao, Nano Lett. **15**, 4013 (2015).
[9] W. Zhang, Z. Huang, W. Zhang, and Y. Li, Nano Res. **7**, 1731 (2014).
[10] X. Chia, A. Adriano, P. Lazar, Z. Sofer, J. Luxa, and M. Pumera, Adv. Funct. Mater. **26**, 4306 (2016).
[11] Z. Y. Zhu, Y. C. Cheng, and U. Schwingenschlögl, Phys. Rev. B **84**, 153402 (2011).
[12] G.-B. Liu, W.-Y. Shan, Y. Yao, W. Yao, and D. Xiao, Phys. Rev. B **88**, 085433 (2013).
[13] D. Xiao, G.-B. Liu, W. Feng, X. Xu, and W. Yao, Phys. Rev. Lett. **108**, 196802 (2012).

[14] M. A. Cazalilla, H. Ochoa, and F. Guinea, Phys. Rev. Lett. **113**, 077201 (2014).

[15] R.-L. Chu, X. Li, S. Wu, Q. Niu, W. Yao, X. Xu, and C. Zhang, Phys. Rev. B **90**, 045427 (2014).

[16] Z. Gong, G.-B. Liu, H. Yu, D. Xiao, X. Cui, X. Xu, and W. Yao, Nat. Commun. **4**, 2053 (2013).

[17] K. Gong, L. Zhang, D. Liu, L. Liu, Y. Zhu, Y. Zhao, and H. Guo, Nanotechnology **25**, 435201 (2014).

[18] W. Yao, E. Wang, H. Huang, K. Deng, M. Yan, K. Zhang, K. Miyamoto, T. Okuda, L. Li, Y. Wang, H. Gao, C. Liu, W. Duan, and S. Zhou, Nat. Commun. **8**, 14216 (2017).

[19] C. Cheng, J.-T. Sun, X.-R. Chen, and S. Meng, Sci. Bull. **63**, 85 (2018).

[20] J. Schliemann, Rev. Mod. Phys. **89**, 011001 (2017).

[21] B. A. Bernevig, J. Orenstein, and S.-C. Zhang, Phys. Rev. Lett. **97**, 236601 (2006).

[22] M. I. Dyakonov and V. I. Perel, Sov. Phys. Solid State **13**, 3023 (1972).

[23] P. Altmann, M. P. Walser, C. Reichl, W. Wegscheider, and G. Salis, Phys. Rev. B **90**, 201306(R) (2014).

[24] J. P. Perdew, K. Burke, and M. Ernzerhof, Phys. Rev. Lett. **77**, 3865 (1996).

[25] T. Ozaki, H. Kino, J. Yu, M. J. Han, N. Kobayashi, M. Ohfuti, F. Ishii, T. Ohwaki, H. Weng, and K. Terakura, OPENMX, http://www.openmx-square.org/.

[26] N. Troullier and J. L. Martins, Phys. Rev. B **43**, 1993 (1991).

[27] T. Ozaki, Phys. Rev. B **67**, 155108 (2003).

[28] T. Ozaki and H. Kino, Phys. Rev. B **69**, 195113 (2004).

[29] G. Theurich and N. A. Hill, Phys. Rev. B **64**, 073106 (2001).

[30] M. A. U. Absor and F. Ishii, Phys. Rev. B **99**, 075136 (2019).

[31] M. A. U. Absor and F. Ishii, Phys. Rev. B **100**, 115104 (2019).

[32] C. Freysoldt, B. Grabowski, T. Hickel, J. Neugebauer, G. Kresse, A. Janotti, and C. G. Van de Walle, Rev. Mod. Phys. **86**, 253 (2014).

[33] M. Zulfiqar, Y. Zhao, G. Li, S. Nazir, and J. Ni, J. Phys. Chem. C **120**, 25030 (2016).

[34] W. Zhang, H. T. Guo, J. Jiang, Q. C. Tao, X. J. Song, H. Li, and J. Huang, J. Appl. Phys. **120**, 013904 (2016).

[35] E. I. Rashba, Sov. Phys. Solid State **2**, 1109 (1960).

[36] G. Dresselhaus, Phys. Rev. **100**, 580 (1955).

[37] M. A. U. Absor, I. Santoso, Harsojo, K. Abraha, F. Ishii, and M. Saito, Phys. Rev. B **96**, 115128 (2017).

[38] H.-P. Komsa and A. V. Krasheninnikov, Phys. Rev. B **91**, 125304 (2015).

[39] J.-Y. Noh, H. Kim, and Y.-S. Kim, Phys. Rev. B **89**, 205417 (2014).

[40] W.-F. Li, C. Fang, and M. A. van Huis, Phys. Rev. B **94**, 195425 (2016).

[41] H.-P. Komsa, S. Kurasch, O. Lehtinen, U. Kaiser, and A. V. Krasheninnikov, Phys. Rev. B **88**, 035301 (2013).

[42] Q. Chen, H. Li, S. Zhou, W. Xu, J. Chen, H. Sawada, C. S. Allen, A. I. Kirkland, J. C. Grossman, and J. H. Warner, ACS Nano **12**, 7721 (2018).

[43] S. Wang, G.-D. Lee, E. Yoon, and J. H. Warner, ACS Nano **10**, 5419 (2016).

[44] I. I. Fishchuk, A. Kadashchuk, A. Bhoolokam, A. de Jamblinne de Meux, G. Pourtois, M. M. Gavrilyuk, A. Köhler, H. Bässler, P. Heremans, and J. Genoe, Phys. Rev. B **93**, 195204 (2016).

[45] See Supplemental Material at http://link.aps.org/supplemental/10.1103/PhysRevB.101.155410 for the calculated results of the spin-split bands along the Γ-*X* line with a larger supercell.

[46] L. Hu, H. Huang, Z. Wang, W. Jiang, X. Ni, Y. Zhou, V. Zielasek, M. G. Lagally, B. Huang, and F. Liu, Phys. Rev. Lett. **121**, 066401 (2018).

[47] M. P. Walser, C. Reichl, W. Wegscheider, and G. Salis, Nat. Phys. **8**, 757 (2012).

[48] C. Schönhuber, M. P. Walser, G. Salis, C. Reichl, W. Wegscheider, T. Korn, and C. Schüller, Phys. Rev. B **89**, 085406 (2014).

[49] A. Sasaki, S. Nonaka, Y. Kunihashi, M. Kohda, T. Bauernfeind, T. Dollinger, K. A. Richter, and J. Nitta, Nat. Nanotechnol. **9**, 703 (2014).

[50] J. Ishihara, Y. Ohno, and H. Ohno, Appl. Phys. Express **7**, 013001 (2014).

[51] L. L. Tao and E. Y. Tsymbal, Nat. Commun. **9**, 2763 (2018).

[52] C. Autieri, P. Barone, J. Sławińska, and S. Picozzi, Phys. Rev. Mater. **3**, 084416 (2019).

[53] M. A. U. Absor, F. Ishii, H. Kotaka, and M. Saito, Appl. Phys. Express **8**, 073006 (2015).

[54] H. Ai, X. Ma, X. Shao, W. Li, and M. Zhao, Phys. Rev. Mater. **3**, 054407 (2019).

[55] S. Vajna, E. Simon, A. Szilva, K. Palotas, B. Ujfalussy, and L. Szunyogh, Phys. Rev. B **85**, 075404 (2012).

[56] N. Yamaguchi and F. Ishii, Appl. Phys. Express **10**, 123003 (2017).

[57] J. Rudge, H. Xu, J. Kolthammer, Y. K. Hong, and B. C. Choi, Rev. Sci. Instrum. **86**, 023703 (2015).

[58] K. F. Mak, K. L. McGill, J. Park, and P. L. McEuen, Science **344**, 1489 (2014).

[59] A. V. Kuklin and H. Ågren, Phys. Rev. B **99**, 245114 (2019).

[60] J. M. Gonzalez and I. I. Oleynik, Phys. Rev. B **94**, 125443 (2016).

[61] S. Horzum, D. Çakır, J. Suh, S. Tongay, Y.-S. Huang, C.-H. Ho, J. Wu, H. Sahin, and F. M. Peeters, Phys. Rev. B **89**, 155433 (2014).